Potassium conductance dynamics confer robust spike-time precision in a neuromorphic model of the auditory brain stem

John H. Wittig, Jr. and Kwabena Boahen

J Neurophysiol 110:307-321, 2013. First published 3 April 2013;
doi: 10.1152/jn.00433.2012

J Neurophysiol 110: 307–321, 2013.
First published April 3, 2013; doi:10.1152/jn.00433.2012.

Potassium conductance dynamics confer robust spike-time precision in a neuromorphic model of the auditory brain stem

John H. Wittig, Jr.[1] and Kwabena Boahen[2]

[1]*Laboratory of Neuropsychology, National Institute of Mental Health, Bethesda, Maryland; and* [2]*Bioengineering Department, Stanford University, Stanford, California*

Submitted 23 May 2012; accepted in final form 1 April 2013

Wittig JH Jr, Boahen K. Potassium conductance dynamics confer robust spike-time precision in a neuromorphic model of the auditory brain stem. *J Neurophysiol* 110: 307–321, 2013. First published April 3, 2013; doi:10.1152/jn.00433.2012.—A fundamental question in neuroscience is how neurons perform precise operations despite inherent variability. This question also applies to neuromorphic engineering, where low-power microchips emulate the brain using large populations of diverse silicon neurons. Biological neurons in the auditory pathway display precise spike timing, critical for sound localization and interpretation of complex waveforms such as speech, even though they are a heterogeneous population. Silicon neurons are also heterogeneous, due to a key design constraint in neuromorphic engineering: smaller transistors offer lower power consumption and more neurons per unit area of silicon, but also more variability between transistors and thus between silicon neurons. Utilizing this variability in a neuromorphic model of the auditory brain stem with 1,080 silicon neurons, we found that a low-voltage-activated potassium conductance (g_{KL}) enables precise spike timing via two mechanisms: statically reducing the resting membrane time constant and dynamically suppressing late synaptic inputs. The relative contribution of these two mechanisms is unknown because blocking g_{KL} in vitro eliminates dynamic adaptation but also lengthens the membrane time constant. We replaced g_{KL} with a static leak in silico to recover the short membrane time constant and found that silicon neurons could mimic the spike-time precision of their biological counterparts, but only over a narrow range of stimulus intensities and biophysical parameters. The dynamics of g_{KL} were required for precise spike timing robust to stimulus variation across a heterogeneous population of silicon neurons, thus explaining how neural and neuromorphic systems may perform precise operations despite inherent variability.

silicon neuron; phase locking; bushy cells; g_{KL}; heterogeneity

AUDITORY NERVE AXONS DIVERGE in the cochlear nuclei to excite multiple cell types that integrate and process different aspects of sound (Young and Oertel 2004). Nerve fiber spikes encode both the intensity and phase of acoustic energy in a narrow band of spectrum, whereas spikes in their targets are skewed toward encoding either intensity or phase (reviewed in Oertel et al. 2011). A phenomenal example of the latter comes from bushy cells, whose spikes encode the phase of low-frequency tones with greater temporal precision than their inputs (Joris et al. 1994a). Bushy cells contribute to the neural circuits for localizing sound sources based on differences of sound pressure level and phase (Yin 2002). At elevated sound levels these cells eschew information about stimulus intensity: they fire exactly one precisely timed spike each stimulus cycle over more than a 20-decibel range of sound pressure level (dB SPL). This intensity-invariant spike-time precision and spike-count reliability is consistent across a heterogeneous population of bushy cells that includes at least two distinct subtypes (Joris et al. 1994a). For predator or prey, reliably localizing an unseen object as it gets very close and thus very loud could be critical to survival.

A key biophysical specialization that enables spike-time precision in bushy cells is a low-voltage-activated potassium conductance (Manis and Marx 1991), g_{KL}, which improves timing via at least two mechanisms: it makes the membrane react quickly to synaptic inputs (fast membrane time constant) by statically conducting current when the neuron is at rest (Oertel 1983), and it reduces the effectiveness of tardy synaptic inputs (which could otherwise cause a poorly timed spike) by dynamically increasing conductance during stimulation (Gittelman and Tempel 2006; Kalluri and Delgutte 2003; Xu-Friedman and Regehr 2005a, 2005b). The relative contribution of these two mechanisms is unknown because blocking g_{KL} in vitro eliminates dynamic adaptation of the membrane conductance but also increases the resting membrane time constant. Furthermore, both mechanisms rely on the interaction between g_{KL}'s magnitude and synaptic conductances, yet maximum g_{KL} levels vary significantly between individual bushy cells, as do the number of auditory nerve inputs to each cell (Cao and Oertel 2010). Nevertheless, 75% of bushy cells most sensitive to low-frequency tones (<700 Hz) exhibit spike-time precision (Joris et al. 1994a). Therefore, the biophysical specializations that enable this phenomenon must compensate for some aspects of cell-to-cell variation (Goaillard et al. 2009) or be insensitive to it (Prinz et al. 2003a).

In this article we present a novel computational model of a bushy cell to address two questions regarding its response to sound: what is the relative contribution of g_{KL}'s static and dynamic components, and how is cell-to-cell variation in conductance magnitudes and innervation patterns counteracted? We examined g_{KL}'s role in spike-time precision using a neuromorphic model that emulates membrane properties of 1,080 bushy cells in real time (Wittig 2010). The custom-designed silicon microchip is 11.3 mm^2 and consumes 3.5 mW of power while emulating 10% of the cat's auditory brain stem with 544,692 transistors and a total of 4,410 silicon neurons. Our silicon bushy cell simulations use 10,000 times less power and are up to 100 times faster than the same simulations in software, enabling us to compare responses across a wide range of stimulus frequencies and intensities while varying several key model parameters. Our results demonstrate that g_{KL}'s static contribution to reducing the membrane time con-

Address for reprint requests and other correspondence: J. H. Wittig, Jr., Laboratory of Neuropsychology, National Institute of Mental Health, 49 Convent Dr., Bldg. 49, Rm. 1B80, Bethesda, MD 20892 (e-mail: john.wittig@nih.gov).

stant is sufficient for spike-time precision over a moderate range of stimulus intensities and number of synaptic inputs. The dynamics of g_{KL} do not substantially increase the level of precision, but instead make that precision impervious to changes in stimulus intensity or biophysical parameters over a wide range. This holds across a heterogeneous population of more than 1,000 silicon bushy cells and provides insight into the phenomenology of other g_{KL}-expressing neurons in the peripheral auditory system.

MATERIALS AND METHODS

Silicon Bushy Cell: Design Overview

There were two discrete phases to developing the hardware neuron model: before and after the circuit was committed to silicon. The first phase involved designing custom circuits to solve a simplified version of a neuron's conductance equation, whereas the second phase involved tuning voltages supplied to the circuit until it yielded the desired conductance equation characteristics. Once tuned, the circuit was probed in real time using a combination of voltage sources (to mimic current- or voltage-clamp inputs), an oscilloscope (to measure time-varying membrane potential and conductance levels), and a personal computer linked via the universal serial bus (to send and receive spikes). The following sections outline the design of the bushy cell circuit and the real-time interface to the fabricated microchip.

Conductance Equation Simplifications

A power-efficient analog circuit solves the neuron's conductance equation continuously in real time. Each transistor is biased to operate in a low-current regime (10^{-12} to 10^{-9} A), where changes in voltage at its gate cause exponential changes in current passing though the transistor (Mead 1989). We exploited this exponential relationship to formulate simple mathematical equations mimicking aspects of the neuron's conductance equation that are solved by the ebb and flow of current through transistors representing the outputs of each equation (Fig. 1*A*). Following the conductance-based design of a software bushy cell model (*Eq. 1*; from Rothman and Manis 2003c), our silicon model computes currents passing though several voltage-dependent channels and takes into account the reversal potential of each conductance (*Eq. 2*).

$$\left(\frac{C_m}{g_H + g_{KH} + g_{KL} + g_{NA} + g_{SYN}}\right)\frac{\partial V_{mem}}{\partial t} + V_{mem} = \left(\frac{g_H \cdot E_H + (g_{KH} + g_{KL}) \cdot E_K + g_{NA} \cdot E_{NA} + g_{SYN} \cdot E_{SYN} + I_{EXT}}{g_H + g_{KH} + g_{KL} + g_{NA} + g_{SYN}}\right) \quad (1)$$

$$\left(\frac{u_T}{\kappa}\right)\left(\frac{C_m}{I_{g_H} + I_{g_{KH}} + I_{g_{KL}}}\right)\frac{\partial I_{mem}}{\partial t} + I_{mem} = \left(\frac{I_{g_H} \cdot I_{E_H} + (I_{g_{NA}} + I_{g_{SYN}} + I_{g_{EXT}}) \cdot I_{E_{NA}}}{I_{g_H} + I_{g_{KH}} + I_{g_{KL}}}\right) \quad (2)$$

In the silicon model, I_{mem} is the time-varying current flow through a transistor (Fig. 1*A*, indicated by an asterisk) that represents the fluctuating membrane voltage of the bushy cell. u_T and κ are constants used to model a transistor's voltage-dependent currents (Mead 1989; Wittig 2010); C_m is the capacitance representing that of the bushy cell membrane; I_{E_H} is a static current (flowing through transistor E_H) that represents the reversal potential of the hyperpolarization-activated mixed-cation current (modulated by g_H); the reversal potential of potassium is treated as 0 in the circuit and is omitted from the equation; $I_{E_{NA}}$ is a constant current that represents the reversal potential of sodium; $I_{g_{EXT}}$ is an externally controlled conductance used to implement depolarizing current-clamp stimuli; $I_{g_{KH}}$ peaks briefly in acknowledgement of a spike but is otherwise 0; I_{g_H}, $I_{g_{KL}}$, $I_{g_{NA}}$, and $I_{g_{SYN}}$ (Fig. 1*A*, outputs of labeled subcircuits) represent the bushy cell's time- and/or voltage-dependent conductances, which are designed to compute the following equations:

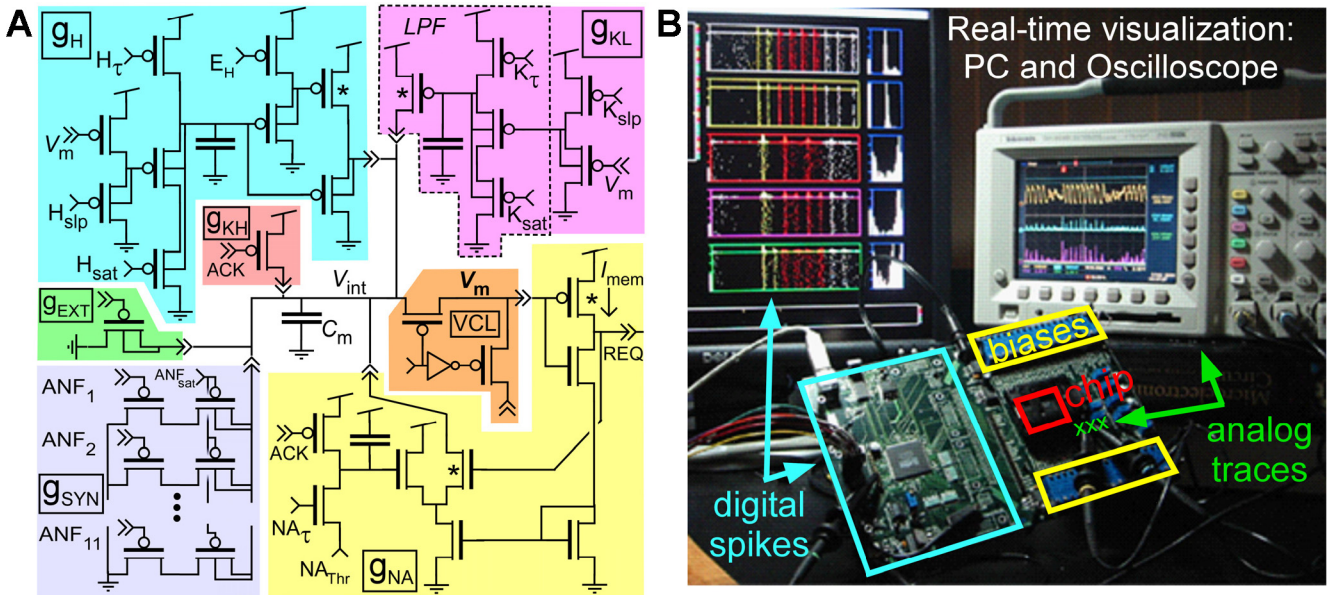

Fig. 1. Silicon bushy cell circuit and neuromorphic chip test setup. *A*: schematic of the analog complementary metal-oxide-semiconductor (CMOS) circuit that implements the bushy cell conductance equation. V_m, the analog membrane voltage, continuously drives the hyperpolarization-activated cation conductance (g_H), low-voltage-activated potassium conductance (g_{KL}), and sodium conductance (g_{NA}) circuits. REQ, the digital spike request, is acknowledged by ACK, which transiently drives the spike-resetting potassium conductance (g_{KH}) and temporarily inactivates g_{NA}. ANF_i, the auditory nerve inputs, are digital pulses, extended to 50 μs and low-pass filtered before driving the synaptic conductance (g_{SYN}). g_{EXT}, the externally controlled transistor, drives excitatory current-clamp stimulation. Currents produced by these conductances are integrated on V_{int}, which can be isolated from V_m by VCL, the voltage-clamp circuitry. The low-pass filter building block is outlined (LPF). *B*: the fabricated microchip consumes 3.5 mW of power and is housed on a custom-designed printed circuit board that supplies bias voltages to its circuits and facilitates real-time communication with test equipment.

$$\left(\frac{u_T}{\kappa}\right)\left(\frac{C_H}{I_{H_\tau}}\right)\frac{\partial I_{g_H}}{\partial t} + I_{g_H} = \left(\frac{I_{off}^2}{I_{H_\tau}}\right)\left(\frac{I_{H_{slp}} \cdot I_{H_{sat}}}{I_{off} \cdot I_{H_{slp}} + I_{H_{sat}} \cdot I_{mem}}\right)\left(\frac{I_{off}}{I_{E_H}}\right) \quad (3)$$

$$\left(\frac{u_T}{\kappa}\right)\left(\frac{C_K}{I_{K_\tau}}\right)\frac{\partial I_{g_{KL}}}{\partial t} + I_{g_{KL}} = \left(\frac{I_{off}^2}{I_{K_\tau}}\right)\left(\frac{I_{mem} \cdot I_{K_{sat}}}{I_{off} \cdot I_{mem} + I_{K_{sat}} \cdot I_{K_{slp}}}\right) \quad (4)$$

$$I_{g_{NA}} = \frac{I_{mem}^3}{I_{off}\left(2I_{mem} + I_{NA_{thr}} + I_{on} \cdot u(t - t_{ACK}) \cdot e^{-(t-t_{ACK})/\tau_{NA}}\right)} \quad (5)$$

$$I_{g_{SYN}} = I_{ANF_{sat}} \cdot \sum_n u\left(t - t_{ANF_n}\right) \cdot e^{-(t-t_{ANF_n})/\tau_{ANF}} \quad (6)$$

Both I_{g_H} and $I_{g_{KL}}$ are sigmoidal functions of I_{mem} (right-hand side of *Eqs. 3* and *4*; slopes and saturation levels adjusted with $I_{H_{slp}}$, $I_{K_{slp}}$, $I_{H_{sat}}$, and $I_{K_{sat}}$) that are low-pass filtered according to the time constants set by the size of capacitors C_H and C_K and the magnitude of currents I_{H_τ} and I_{K_τ}. I_{off} is the minimum current through a transistor. The sodium conductance, $I_{g_{NA}}$, increases with the square of I_{mem} once the threshold level set by $I_{NA_{thr}}$ is surpassed. $I_{g_{NA}}$ activates instantaneously (i.e., no low-pass filtering) and inactivates briefly after the bushy cell spikes [t_{ACK} is the timing of the digital pulse that acknowledges a spike has occurred; $u(t)$ is a unit step function; I_{on} is the maximum current through a transistor]. The postsynaptic conductance ($I_{g_{SYN}}$) is the summed response to auditory nerve spikes (digital pulses occurring at times t_{ANF_n}) that are low-pass filtered (time constant τ_{ANF}) and adjusted to the synaptic strength set by $I_{ANF_{sat}}$.

The circuit's conductance equation is simplified relative to the full equation (compare *Eqs. 1* and *2*). The simplified equation required fewer transistors, which reduces its susceptibility to transistor variability (de Gyvez and Tuinhout 2004) and increases the number of circuits that will fit on a single microchip. We made four main simplifications when implementing the conductance equation with transistors and capacitors: *1*) The conductances' voltage dependence captured their relative amplitudes rather than precisely matching magnitudes at each potential (see RESULTS and Fig. 2, *A* vs. *B*). *2*) The conductances' activation kinetics were first order with voltage-independent time constants instead of third or fourth order and voltage dependent. *3*) Excitatory postsynaptic conductances were modeled with instantaneous rise and exponential decay (i.e., also first-order kinetics) without any form of synaptic plasticity. *4*) The neuron's membrane potential was modeled with a single equipotential compartment. Details of our simplifying design choices and their rationales are summarized in Table 1. These rationales were validated by the model's faithful reproduction of a bushy cell's intracellular response to current injection (see Fig. 2*B*), its average spike rate during stimulation by low- and high-frequency pure tones (see Fig. 2*D*), its frequency-dependent decline in vector strength (see Fig. 2*G*), and its intensity-invariant spike-time precision and spike-count reliability (see Fig. 3*A*).

Theoretical Circuit and Chip Testing

Schematic to microchip. Translating the theoretical circuit to a usable microchip required several steps. We confirmed functionality of the circuit and refined our design by simulating the interaction between transistors in software (Tanner Tools; Tanner Research, Monrovia, CA). We then converted the circuit schematic to a physical layout of transistors and wires conforming to Taiwan Semiconductor Manufacturing Company (TSMC)'s 0.25-μm complementary metal-oxide-semiconductor (CMOS) fabrication processes. The layout for a single cell's analog circuit was replicated and tiled using custom software to create a microchip with 1,080 bushy cell circuits and ~4,000 other cochlear nucleus neurons (Wittig 2010). Circuitry was added to communicate digital spike events (Boahen 2004) and analog currents to or from the chip. Forty copies of the microchip were fabricated by TSMC via the MOSIS educational program. We designed a printed circuit board to house the microchip and interface with test equipment (Fig. 1*B*).

Tuning model conductances. The voltage biases supplied to the chip were adjusted iteratively until the circuit's conductances best matched those expected for a biological bushy cell at physiological temperature. Conductance magnitudes and kinetics are often measured at room temperature in vitro (e.g., Rothman and Manis 2003a, 2003b) but have a strong temperature dependence (Cao et al. 2007; Rothman and Manis 2003a). We therefore used an established software bushy cell model with conductance magnitudes and kinetics adjusted for physiological temperature (Rothman and Manis 2003c) to estimate the biological bushy cell's in vivo conductances curves (see Fig. 2*A*). We also used the software model to confirm reproducibility of all results reported for the silicon bushy cell (see RESULTS and DISCUSSION). The time constants for each of the silicon model's conductances were measured and adjusted in voltage clamp. g_H and g_{KL} magnitudes were adjusted in current clamp while the resting membrane time constant was measured. The reversal potential (E_H) of the current passed by g_H was adjusted in current clamp to set the

Table 1. *Simplifying design choices and rationales for the silicon bushy cell model*

Parameter	Biological Bushy Cell	Silicon Bushy Cell	Justification
Spatial homogeneity of membrane potential	Membrane potential nonuniform across dendrites, soma, and axon hillock	Single membrane potential computed for entire cell	Multicompartment model (Spirou et al. 2005) had similar properties to single-compartment models (Rothman and Manis 2003b; Rothman and Young 1996)
Reversal potentials	Specific reversal potentials for each conductance: $E_K = -85$ mV, $E_H = -40$ mV, $E_{NA} = 50$ mV, $E_{SYN} = 0$ mV	Relative reversal potentials: $E_K = 0 < E_H < E_{SYN} = E_{NA}$	Reversal potentials not measured in vivo, and measurement has some variability within and between cells
Membrane time constant	Membrane capacitance divided by sum of all conductances	Exclude ultrafast conductances g_{NA} and g_{SYN}	Conductances active for <0.1 ms should not appreciably affect integration
g_{KL} *G-V* curve	Boltzman function, increasing with membrane potential	Proportional to V_{mem}, with saturation at upper bound	Linear approximation in the region of the resting potential appears reasonable based on average biological *G-V* curves (see Fig. 2*A*)
g_H *G-V* curve	Boltzman function, decreasing with membrane potential	Inversely proportional to V_{mem}	Membrane potential rarely hyperpolarized enough in vivo to reach g_H saturation
Conductance time constants	Voltage-dependent activation kinetics of g_{NA}, g_{KL}, and g_H fit by bell-shaped curve (Rothman and Manis 2003a)	Activation kinetics fixed at temperature-adjusted mean value for each conductance	Functional range of membrane potential restricted in vivo

g_H, hyperpolarization-activated cation conductance; g_{KL}, low-voltage-activated potassium conductance; g_{NA}, sodium conductance; g_{SYN}, synaptic conductance; *E*, reversal potential; *G-V*, conductance-voltage; V_{mem}, membrane voltage.

resting membrane potential. Conductance-voltage curves were then measured for all conductances and compared against biological curves as described in RESULTS (see Fig. 2*B*). A similar process was used to find appropriate voltages when augmenting the model (see Fig. 2*C*).

Sending and receiving spikes. A personal computer running C++ code interfaced with the chip via the universal serial bus to send and receive spikes and provide real-time feedback of spiking behavior. The timing of auditory nerve spikes was computed using a stochastic software model (Sumner et al. 2003) that can mimic the responses of nerve fibers with low, medium, or high spontaneous rates (LSR, MSR, and HSR). Biological bushy cells are predominantly innervated by HSR fibers but also receive inputs from LSR and MSR fibers (Liberman 1991). Our initial model of an average bushy cell was driven by 11 auditory nerve fibers: 1 LSR, 1 MSR, and 9 HSR. The silicon bushy cell circuit included 11 independent synaptic subcircuits so that concurrent excitatory postsynaptic currents (EPSCs) could sum. The amplitude and time course implemented by each synapse circuit was different (approximately ranging ±10% of the mean values) due to the inherent variability of analog circuits (see Fig. 7*A*). When cell-to-cell variability was examined, the reference bushy cell model was driven by 4 LSR, 4 MSR, and 8 HSR fibers. To drive the cell with more than 11 auditory nerve inputs, we virtually routed spikes from multiple auditory nerve fibers onto each hardware synapse. When 2 spikes occurred within 50 μs on the same synapse (up to 10% of spikes with 32 auditory nerve fiber inputs at 120 dB SPL), the second spike's EPSC was effectively depressed (reduction in amplitude) because the synapse circuit required 50 μs to fully reset between spikes. We modeled the response of a high best-frequency bushy cell by driving our average bushy cell model with simulated auditory nerve fibers most sensitive to 8-kHz stimuli. All auditory nerve spike times were computed offline and stored to disk for rapid retrieval during real-time simulations of the silicon bushy cell. During simulations, auditory nerve spikes were digitally routed to the bushy cell's synapse circuitry, and neuronal spikes were digitally routed off chip every 480 ns for visualization and storage on a personal computer.

Acoustic stimulus parameters. The software auditory nerve model was driven with acoustic stimuli designed to mimic stimuli used experimentally (Joris et al. 1994a). Tone bursts (both pure tone and amplitude modulated) were 25 ms in duration, started at the same phase each trial, had 2.5-ms rise and fall times, and had a 25-ms interstimulus interval. Sound pressure amplitude was adjusted to achieve root-mean-squared sound pressures ranging from 40 to 120 dB SPL relative to atmospheric pressure. Stimuli were presented 1,000 times, except when simulating 1,080 silicon neurons, in which case the stimuli were presented 250 times. Spike rates, vector strengths, and entrainment indices were computed from spikes occurring between 10 and 22 ms after the stimulus onset. The lower bound (10 ms) was chosen to accommodate the onset delay of low-frequency fibers (Joris et al. 1994a), and the upper bound was chosen so the analysis window covered an integer number of stimulus cycles (i.e., 3 cycles at 250 Hz is 12 ms).

Comparing vector strength at 70 and 120 db SPL in a single neuron. We used a bootstrap procedure to test the null hypothesis that an individual neuron's vector strength did not change with stimulus intensity (i.e., see Fig. 3*C*). This technique is appropriate when comparing two vector strength measures from the same neuron (Zahar et al. 2009). Spike times from 1,000 stimulus presentations were used to create period histograms, the measured distribution of spike phases for each simulated condition. The vector strengths reported in the text and figures are directly computed from those period histograms. A synthetic period histogram was generated by randomly drawing (with replacement) spike phases from the measured distribution repetitively until the synthetic period histogram had the same number of spike phases as the measured distribution (about 3,000 spike phases). A second synthetic period histogram was generated based on the measured period histogram to be compared (i.e., 70 vs. 120 dB SPL). Vector strengths were computed for the two synthetic period histograms, and the difference was stored. This process was iterated 5,000 times to create a bootstrap distribution of vector strength differences. The 99% confidence interval of the bootstrap distribution was defined to be the interval between the 0.5th and 99.5th percentiles. If this interval did not cover 0, the null hypothesis was rejected and the vector strengths were deemed significantly different at the $P = 0.01$ level (Fisher 1995; Zahar et al. 2009). We also used a bootstrap procedure to compute 99% confidence intervals (bias corrected and accelerated) for vector strength estimates at 70 and 120 dB, separately, to gauge the reliability of the vector strength measure (error bars in Fig. 3*C*). The confidence intervals ranged from 0.003 to 0.048 vector strength units, with bigger intervals for smaller vector strengths.

RESULTS

Isolating g_{KL}'s Static and Dynamic Contributions to Spike-Time Precision

We developed a silicon bushy cell model to determine the relative contribution of g_{KL}'s dynamic and static activation to spike-time precision. Bushy cells are amenable to computational modeling because they have well-characterized voltage-dependent conductances (Cao et al. 2007; Rothman and Manis 2003a), synaptic connectivity (Brawer and Morest 1975; Ryugo and Sento 1991; Spirou et al. 2005), and responses to acoustic stimuli (Blackburn and Sachs 1989; Joris et al. 1994a). We configured the silicon bushy cell with two different settings: one that mimics the characteristics of an average bushy cell with g_{KL} intact, and another with g_{KL} replaced by a static leak. In this section we compare the models' conductance-voltage curves and responses to current injection with those measured in vitro.

Interaction of voltage-dependent conductances in vitro. g_{KL} enhances spike-time precision via two distinct mechanisms, both realized by its voltage-dependent interaction with other conductances (Fig. 2*A*). At the neuron's resting potential (Fig. 2*A*, open triangle), g_{KL} is weakly activated (about 5% of maximum) and yields a hyperpolarizing current that counterbalances the depolarizing current from the hyperpolarization-activated conductance, g_H (Cao and Oertel 2011). The combined conductivity of g_H and g_{KL} at rest imbues the bushy cell with a fast membrane time constant. With moderate depolarization, g_{KL} begins to saturate near its maximum value, and the sodium conductance (g_{NA}) responsible for spike generation activates with a steep voltage dependence. g_{KL}'s dynamic voltage-dependent activation and deactivation near the resting potential as well as its static weak activation at rest contribute to spike-time precision.

The effects of g_{KL}'s resting level and voltage-dependent activation are apparent in the membrane's response to current injection. We simulated the current-clamp response of a bushy cell using a previously validated software model that mimics in vivo bushy cell responses when conductance magnitudes and kinetics have been adjusted for physiological temperatures assuming a Q_{10} of 2 (Rothman and Manis 2003c). The software model's time constant at physiological temperature is 0.2 ms, similar to the time constant of other auditory neurons at physiological temperatures (Klug and Trussell 2006). At the onset of current injection, membrane voltage (V_{mem}) increased rapidly whereas g_{KL} increased with a slight lag due to its activation kinetics (Fig. 2*A*, traces at *right*). Without g_{KL} fully activated during the first few hundred microseconds, the mem-

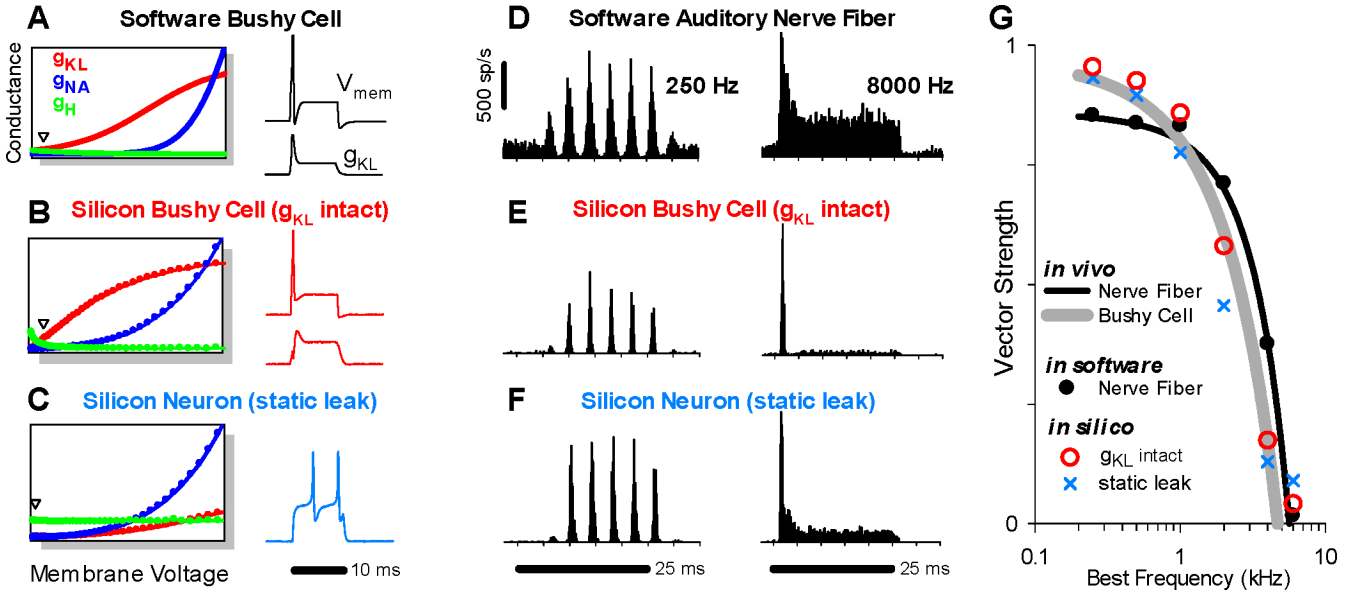

Fig. 2. Silicon bushy cell mimics several acoustic response features with g_{KL} intact or replaced by a static leak. *A–C*: dependence of 3 conductances on bushy cell membrane potential: g_{KL} (red), g_{NA} (blue), and g_H (green). Resting potential is indicated with an open triangle. Response to 10-ms depolarizing current pulse is shown at *right*. The software model's magnitudes and kinetics are based on in vitro measurements, averaged and scaled to account for physiological temperature (Rothman and Manis 2003c). Conductance axis range is 0 to 260 nS. Membrane voltage range is −70 to −35 mV. The silicon model is configured with g_{KL} intact or replaced by a static leak, implemented by reducing g_{KL} and converting g_H into a voltage-independent leak conductance. g_H did not impact the membrane's response to transient stimuli because it activates too slowly (time constant ~50 ms) to dynamically affect spike-time precision during a 10-ms stimulus. In silico parameters are represented by currents. Conductanceaxis axis range is 0 to 150 nA. Membrane voltage range is 0 to 8 μA. *D–F*: peristimulus time histograms of instantaneous spike rate (0.1-ms bins) computed from 1,000 responses to a 25-ms pure tone at 60 dB SPL stimulus (*left*, 250 Hz; *right*, 8,000 Hz) for a software auditory nerve fiber and a silicon bushy cell with g_{KL} intact or replaced by a static leak. Vertical scale bar applies to all histograms. *G*: maximum vector strength across a range of pure tone frequencies.

brane depolarized sufficiently to activate the sodium conductance and initiate a spike. By the end of this onset spike, g_{KL} had activated and counterbalanced the input current to prevent further depolarization of the membrane. At the falling phase of the stimulus, the membrane voltage rapidly dropped below its resting level for ~2 ms until g_{KL} deactivated. The dynamic responses to current onset and offset as well as the fast membrane time constant are signature attributes of g_{KL}-expressing neurons in vitro (Manis and Marx 1991).

Interaction of voltage-dependent conductances in silico. In silico, the bushy cell included three conductances that mimicked the voltage dependence of g_{KL}, g_H, and g_{NA} (Fig. 2*B*). The membrane potential and conductance levels were represented as currents, the natural representation of numerical values in the medium of transistor circuits (Wittig 2010; Wittig and Boahen 2006). The conductance-voltage curves were not exact matches because we implemented a simplified version of the cell's conductance equation (see MATERIALS AND METHODS). The model captured the conductances' relative amplitudes rather than the absolute levels found in biology. For instance, g_{KL} activated at lower membrane voltage values than g_{NA} and was close to saturation when it was surpassed by g_{NA}. Additionally, the curves for g_H and g_{KL} crossed near the neuron's resting potential. The model also included a g_{KH} conductance that was not voltage dependent per se; it was triggered to repolarize the membrane after a spike using digital circuitry. The silicon bushy cell's dynamic response to a depolarizing current pulse mimicked that of its biological inspiration, as did its resting membrane time constant (0.2 ms).

We also configured the silicon neuron model with g_{KL} replaced by a static leak conductance that matched g_{KL}'s resting level but did not change with time or voltage (Fig. 2*C*). We adjusted the leak's magnitude so the neuron's membrane time constant (0.2 ms) matched that with g_{KL} intact (cf. the "frozen-KLT" model of Day et al. 2008). During current injection the membrane potential still rapidly depolarized, but increased current levels evoked multiple spikes during the stimulus on-phase, which did not occur with g_{KL} intact. Therefore, g_{KL}'s dynamics restrict spikes to the stimulus onset in the silicon bushy cell, as would be predicted from the dynamic membrane response of g_{KL}-expressing neurons in vitro (Gittelman and Tempel 2006; Golding et al. 1999; Svirskis et al. 2002; Xu-Friedman and Regehr 2005a, 2005b).

A Fast Membrane Time Constant is Sufficient to Mimic Most Bushy Cell Phenomenology

Biological bushy cells are excited by synaptic inputs from auditory nerve fibers; therefore, we delivered realistic synaptic inputs to the silicon bushy cell using an accurate software model of the auditory nerve (Sumner et al. 2003). When driven by a low-frequency pure tone, biological auditory nerve fibers spike at approximately the same phase each cycle of the sinusoidal input: their spikes phase lock to the stimulus (Johnson 1980). The software auditory nerve fiber accurately captured this phenomenon; a 25-ms, 250-Hz pure tone at 60 dB SPL evoked periodic peaks of instantaneous spike rate (up to 1,200 spikes/s in 0.1-ms bins) at 4-ms intervals with rates dipping as low as 0 spikes/s in between (Fig. 2*D*). The peak rates are largely due to the occurrence of spikes at precisely the same phase of the stimulus each trial, although sometimes more than one spike occurs per stimulus cycle. Vector strength is a metric used to quantify phase-lock precision that ranges

from 0 for no phase locking to 1 when all spikes occur at exactly the same phase of the stimulus. The high spontaneous rate fiber had a vector strength of 0.72. Between stimulus presentations its spontaneous rate was 150 spikes/s (Fig. 2*D*, before 0 and after 30 ms). The model fiber's vector strength and spontaneous rate were within the range observed for high spontaneous rate fibers in vivo.

Enhancement of phase locking to low-frequency stimuli. Bushy cells spike with greater temporal precision than their auditory nerve inputs at low stimulus frequencies (Blackburn and Sachs 1989; Joris et al. 1994a). The model bushy cell accurately captured this phenomenon when driven by 11 auditory nerve fibers with a mix of spontaneous rates (see MATERIALS AND METHODS); it exhibited periodic peaks of instantaneous spike rate, but with narrower widths than those of its inputs (Fig. 2, compare *D* and *E*). The model's vector strength of 0.95 and spontaneous rate of 2.5 spikes/s were within ranges observed for globular bushy cells sensitive to low-frequency pure tones in vivo (Joris et al. 1994a). Like its biological counterpart, the model bushy cell enhanced the spike-time precision of its inputs. The static leak neuron also spikes with greater temporal precision than its auditory nerve inputs at low stimulus frequencies (Fig. 2*F*; vector strength of 0.91), as would be predicted based on theoretical examinations of enhanced phase locking by integrate-and-fire neurons (e.g., Burkitt and Clark 2001). The spike rates for this model were higher than with g_{KL} intact but were still within the range observed in vivo. g_{KL}'s dynamics are not required to mimic the enhancement of spike-time precision at low frequencies; a static leak conductance is sufficient.

Enhancement of onset response to high-frequency stimuli. The auditory nerve and bushy cell models also matched in vivo responses to high-frequency pure tones. Auditory nerve fibers respond to high-frequency pure tones with an initial peak in spike rate (>1,500 spikes/s) that adapts within milliseconds to a steady-state level of ~300 spikes/s (Rhode and Smith 1985). Their spikes do not phase lock to the acoustic stimulus. The auditory nerve model mimicked this phenomenon when stimulated with an 8-kHz, 60-dB pure tone for 25 ms (Fig. 2*D*; vector strength of 0.02). Similarly, the bushy cell model mimicked a prototypical response of globular bushy cells (Fig. 2*E*): it fired a single, precisely timed spike at the onset of sound, paused briefly, and then sustained a low firing rate (cf. onset-locker response in Rhode and Smith 1986). The neuron model with a static leak also exhibited a prototypical bushy cell response to high-frequency sounds, albeit one with a higher sustained activity (Fig. 2*F*). In vivo, bushy cells sometimes exhibit slightly varied responses (Smith et al. 1991, 1993): some have elevated sustained activity and a less prominent onset, like their inputs ("primary-like," likely to be spherical bushy cells), and others have elevated sustained activity but a well-aligned first spike that results in a subsequent trough due to spike refractoriness ("primary-like with notch," likely to be globular bushy cells). g_{KL}'s dynamics are not required to mimic the bushy cell's characteristic response to high-frequency sounds: a static leak conductance is sufficient.

Graceful degradation of phase locking with increasing stimulus frequency. The bushy cell model's spike-time precision matched in vivo observations for a wide range of stimulus frequencies with g_{KL} intact or replaced by a static leak. The auditory nerve's disparate responses to low- and high-frequency tones (Fig. 2*D*, *left* vs. *right*) represent two extremes of a continuous change in response properties with stimulus frequency. As stimulus frequency increases, auditory nerve responses gradually transition from phase locked to having no correlation with stimulus phase (Johnson 1980). The average vector strength across a population of cat auditory nerve fibers can be described with a continuous function that declines from 0.85 at 200 Hz to near 0 by 6 kHz (Blackburn and Sachs 1989). The average vector strength of a population of cat bushy cells is higher than the auditory nerve's at low frequencies (0.94 at 200 Hz), but is lower than the auditory nerve's above 1 kHz (Fig. 2*G*, compare black and gray lines). A model of cat auditory nerve fibers (Rothman and Young 1996) matched the biological curve at six specific frequencies (black dots fall on black line). When driven by 11 simulated cat fibers, the silicon bushy cell accurately followed the observed pattern of low-frequency enhancement and high-frequency degradation of spike-time precision relative to its auditory nerve inputs (red circles follow gray line), and so did the silicon neuron with a static leak (blue crosses). At most frequencies the static leak model's vector strength was slightly lower than that with g_{KL} intact, but both exhibited precision within the range observed in vivo. Therefore, the bushy cell's fast membrane time constant, rather than g_{KL}'s voltage-dependent dynamics, suffices to explain many of the bushy cell's characteristic response features. Furthermore, the silicon model's successful mimicry of a range of acoustic responses validates its simplified conductance-voltage curves as well as the configuration of its synaptic inputs.

Intensity Dependence of Spike-Time Precision

As a quiet sound increases in intensity, the spike rates of auditory nerve fibers and bushy cells increase from their spontaneous levels and the timing of their spikes becomes more precise. At higher intensities, the responses of auditory nerve fibers continue to change with stimulus intensity, whereas bushy cells maintain a constant spike rate and spike-time precision. This intensity-invariant spike-time precision was documented in vivo by varying the intensity of a pure tone stimulus and measuring three response features: spike rate, vector strength, and entrainment index (Joris et al. 1994a, 1994b). The entrainment index conveys how reliably a neuron spikes on a cycle-by-cycle basis: a measure of spike-count reliability. It is the proportion of total interspike intervals within 1 plus or minus half of the stimulus period and ranges from 1 for a neuron that spikes once (and only once) each stimulus cycle to 0 for a neuron that always skips consecutive cycles or spikes several times throughout each cycle (whereas a burst of spikes separated by more than half a period would yield a non-zero value). As sound intensity increases, auditory nerve fiber spike rates increase to a stable level and then slightly increase or decrease at high intensity levels, whereas their vector strength and entrainment index peak at moderate sound levels and then decline (Cai and Geisler 1996; Joris et al. 1994a; Palmer and Russell 1986). In contrast, bushy cell spike rates initially increase with intensity and then remain fixed over an additional 20 dB SPL, and their vector strength and entrainment index remain nearly ideal (both >0.95) irrespective of intensity (Joris et al. 1994a, 1994b).

Intensity-invariant spike-time precision requires dynamics of g_{KL}. Like its biological inspiration, the model bushy cell exhibited intensity-invariant spike-time precision, but only with g_{KL}'s dynamics included (Fig. 3*A*). The model's vector strength with g_{KL} intact or replaced by a static leak was higher than that of its auditory nerve inputs for all stimulus intensities (Fig. 3*A*, vector strength). The auditory nerve fibers' vector strength peaked at 0.86 at 70 dB SPL and then gradually declined to between 0.55 and 0.65 as intensity increased to 120 dB SPL, depending on the spontaneous rate of the fiber (compare lines in different shades of gray). In contrast, with g_{KL} intact, the model bushy cell's vector strength increased monotonically with sound intensity to a peak of 0.99 at 75 dB SPL and beyond. Replacing g_{KL} with a static leak had little effect at low and moderate stimulus intensities, where the neuron also achieved nearly ideal vector strength, but was deleterious at high intensities, where its spike-time precision declined like that of its auditory nerve inputs. g_{KL}'s dynamics enabled the bushy cell to maintain nearly ideal phase locking at intensities above 70 dB SPL.

g_{KL}'s dynamics also endowed the neuron with spike-count invariance across stimulus intensities (Fig. 3*A*, Entrainment Index). The auditory nerve fiber's entrainment index peaked at 0.8 at 70 dB SPL and then gradually declined to 0.65 as intensity continued to increase to 120 dB SPL. The bushy cell model with g_{KL} intact or replaced by a static leak enhanced entrainment relative to its auditory nerve inputs for all intensities greater than 60 dB SPL. With g_{KL} intact, the bushy cell maintained nearly ideal entrainment as stimulus intensity increased from 70 to 120 dB SPL (index between 0.97 and 0.99), whereas with a static leak its entrainment index steadily decreased from the peak value at 70 dB SPL (0.99) as intensity increased to 120 dB SPL (0.86). This decline coincided with an increased likelihood of multiple spikes per cycle, as evidenced in the neuron's increasing spike rate (Fig. 3*A*). g_{KL}'s dynamics are necessary for intensity-invariant spike-time precision and spike-count reliability in bushy cells sensitive to low stimulus frequencies.

Spike rasters from model auditory nerve fibers and bushy cells with g_{KL} or a static leak offer insight into why g_{KL}'s dynamics are important for intensity-invariant spike-time precision (Fig. 3*B*). At 70 dB SPL, the group of 11 auditory nerve fibers that stimulated the bushy cell spiked throughout 1.5 ms of each 4-ms stimulus cycle. With this synaptic input, the bushy cell responded with a precisely timed spike each cycle whether g_{KL} was intact or replaced by a static leak; g_{KL}'s static contribution to reducing the membrane time constant was sufficient for precise spike timing. At 120 dB SPL, the group of nerve fibers collectively spike for a longer interval each cycle, ~2 ms of each 4-ms stimulus cycle. The additional late-phase spikes come from LSR and MSR fibers that exhibit more jitter during each cycle, as well as HSR fibers that fire twice during a stimulus cycle (Fig. 3*B*, single HSR ANF), a phenomenon known as peak splitting (Cai and Geisler 1996). With this synaptic input the model bushy cell continued to fire a single, precisely timed spike each stimulus cycle with g_{KL} intact, but with a static leak it occasionally also fired an additional off-phase spike. Although a reduced membrane time constant imbued the bushy cell with more precisely timed spikes than its inputs, g_{KL}'s dynamics were required to limit subsequent ill-timed responses.

We observed intensity-invariant spike-time precision irrespective of the spontaneous rates of the nerve fibers used to drive the silicon bushy cell (Fig. 3*C*). We calculated the change in vector strength from its peak value at 70 dB SPL to the value at 120 dB SPL. The group of 11 auditory nerve fibers exhibited

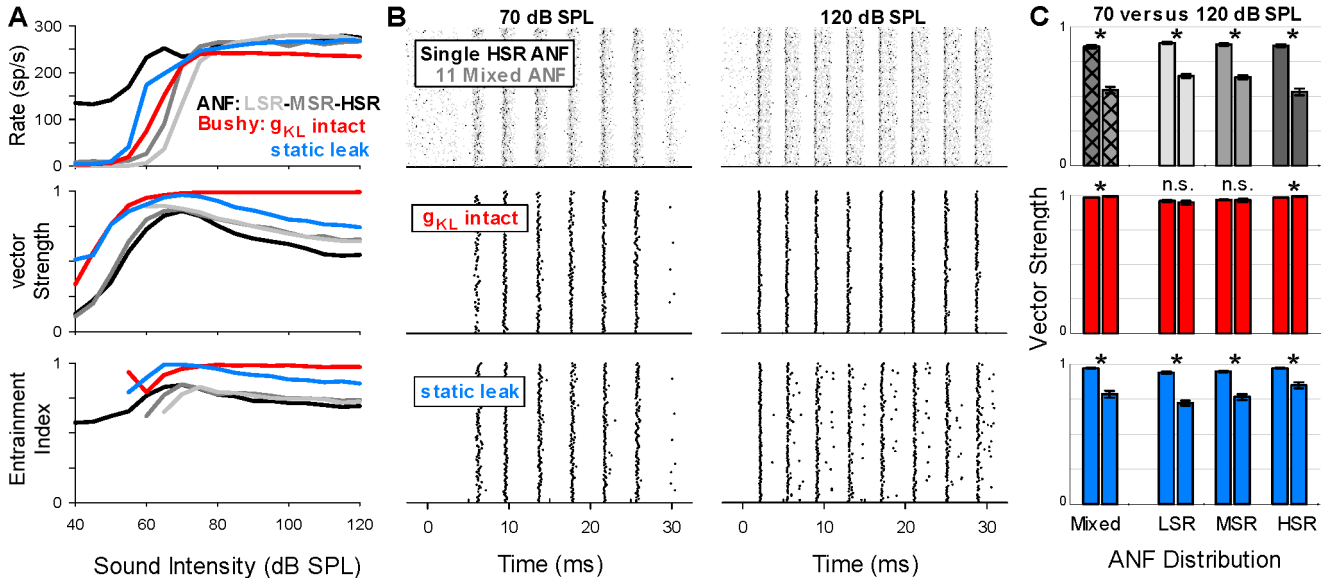

Fig. 3. Silicon bushy cell mimics intensity-invariant spike-time precision and spike-count reliability with g_{KL} intact, but not with a static leak. *A*: spike rate, vector strength, and entrainment index vs. intensity of a 250-Hz pure tone stimulus. Each data point is computed from 1,000 simulated presentations of a 25-ms pure tone at each intensity level (every 5 dB). Results are shown for a silicon bushy cell with g_{KL} intact and replaced by a static leak as well as the low-, medium-, and high-spontaneous rate auditory nerve fibers (ANF: LSR, MSR, HSR) that drives it. Vector strength and entrainment index are computed only if 10 or more spikes or intervals occurred. *B*: spike rasters of the first 100 trials. Mixed ANF distribution includes 1 LSR, 1 MSR, and 9 HSR fibers. *C*: vector strength at 70 and 120 dB SPL of ANF (*top*), bushy cell with g_{KL} intact (*middle*), and bushy cell with g_{KL} replaced by a static leak (*bottom*) for different ANF input distributions (mixed or all from the same spontaneous rate category). Error bars indicate 99% confidence intervals for each vector strength estimate. *Significant difference ($P < 0.01$) in vector strength at 70 vs. 120 dB SPL (see MATERIALS AND METHODS); n.s. indicates no significant difference.

a 0.24-to-0.33 drop in vector strength whether it was composed of a mix of spontaneous rates or exclusively composed of low-, medium-, or high-spontaneous rate fibers (Fig. 3*C*, *top*). We used a bootstrap procedure to determine whether the differences in vector strength were significant (see MATERIALS AND METHODS). In each case the decrease in vector strength was statistically significant ($P < 0.01$). In contrast, the neuron with g_{KL} intact maintained (no significant difference) or increased (by 0.007 to 0.009; $P < 0.01$) vector strength across this same 50-dB range irrespective of auditory nerve fiber input type or mix, whereas with a static leak there was a significant drop of 0.12 to 0.22. Intensity-invariant spike-time precision is robust to changes in auditory nerve model parameters and requires g_{KL}'s dynamics.

We replicated the findings from our neuromorphic chip with an established software model of the bushy cell. Although we already validated the silicon model across a wide range of stimulus parameters, we were concerned that the relationship between intensity invariance and g_{KL} dynamics was somehow a consequence of the simplified conductance equation implemented with transistor circuits. Therefore, we replicated the bushy cell simulations in software using an established model described by Rothman and Manis (2003c). We implemented a verbatim copy of their putative bushy cell model, a "type II" cell, using their adjustment of conductance magnitudes and kinetics for physiological temperature, their approximation of synaptic conductances using an alpha wave with a time constant of 0.07 ms, and their unitary synaptic conductance of 17 nS (their "subthreshold" value, which was half the minimum synaptic conductance required to elicit a spike). When driven by 11 auditory nerve fibers with a mix of spontaneous rates (identical to the silicon bushy cell's inputs for 1,000 stimulus presentations), the software bushy cell with g_{KL} intact maintained near-perfect vector strength and entrainment as intensity increased from 70 to 120 dB SPL (vector strength of 0.99 and 0.96 and entrainment index of 1.0 and 0.98, respectively). We then modified the software model by holding g_{KL} fixed at its steady-state level and reducing the unitary synaptic conductance to 14 nS (28 nS was the minimum synaptic conductance required to elicit a spike in this configuration). When g_{KL} was held fixed in the software model, both vector strength and entrainment peaked to near-perfect values and then dropped precipitously as sound intensity increased from 70 to 120 dB SPL (vector strength of 0.99 and 0.62; entrainment index of 1.0 and 0.80). We conclude that intensity-invariant spike-time precision depends on g_{KL}'s dynamics and that the silicon neuron's conductance equation is sufficiently detailed to capture this phenomenon; therefore, we exclusively report results from the silicon bushy cell for all subsequent analyses.

Frequency Dependence of Intensity-Invariant Spike-Time Precision

In vivo, bushy cells exhibit intensity-invariant spike-time precision only when stimulated by low-frequency pure tones. Previous theoretical studies have identified a limited range of stimulus frequencies over which neurons respond differentially with g_{KL} intact or replaced by a static leak (Day et al. 2008; Gai et al. 2009, 2010) and the extent to which the frequency range is related to g_{KL}'s kinetics (Day et al. 2008). We hypothesized that g_{KL}'s kinetics also dictate a limited operating range of stimulus frequencies over which its dynamics confer intensity-invariant spike-time precision. To test this hypothesis, we evaluated the intensity dependence of spike-time precision for a range of stimulus frequencies with g_{KL} intact or replaced by a static leak, and we then compared the synaptic inputs' time course with that of g_{KL}'s activation and deactivation.

Dynamics of g_{KL} are effective over a limited range of pure tone stimulus frequencies. As stimulus frequency increased, the model bushy cell's capacity for intensity-invariant spike-time precision gradually subsided (Fig. 4*A*). At 250 Hz, vector strength with g_{KL} intact decreased by 0.01 from its maximum value as sound intensity increased by 50 dB SPL, whereas vector strength with a static leak decreases by 0.2 over this same range (compare the height of red- and blue-shaded regions at 250 Hz). The dichotomous vector strength ranges between the models held at 500 Hz, but by 1 kHz the silicon bushy cell with g_{KL} intact started showing intensity-dependent decline in spike-time precision (vector strength decreases by 0.13 with g_{KL} intact and by 0.20 with a static leak), and by 2 kHz its decline matched that of the static leak model (0.23 and 0.25, respectively). g_{KL}'s dynamics confer intensity-invariant spike-time precision over a limited operating range of stimulus frequencies.

The limited operating range of intensity-invariant spike-time precision was due to g_{KL}'s kinetics. At low stimulus frequencies, auditory nerve spikes congregated together due to phase locking, which left a few milliseconds of synaptic silence between consecutive cycles (e.g., Fig. 4*B*, no spikes between 11 and 13 ms). During this silence, the model bushy cell's membrane potential rapidly approached its resting level (Fig. 4*C*) and g_{KL} decayed to its resting level within 2 ms (Fig. 4*D*). Each synaptic silence ended with a cacophony of auditory nerve inputs (e.g., Fig. 4*B*, 14 ms), which rapidly depolarized the membrane potential but also activated g_{KL}, permitting a single spike to occur. The delayed increase in g_{KL} suppressed the membrane's response to subsequent late synaptic inputs within the same cycle (Fig. 4*B*, 13 vs. 15 ms). In contrast, with

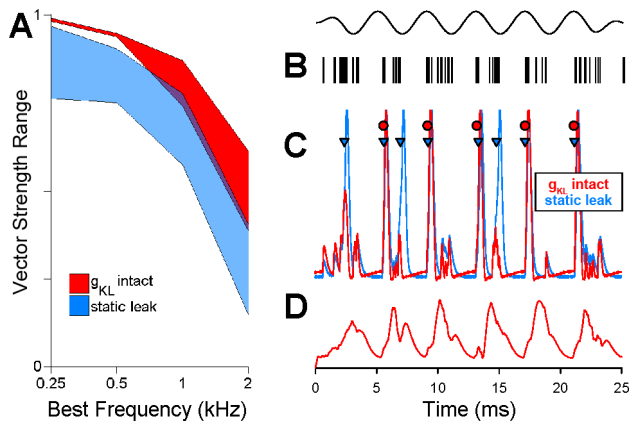

Fig. 4. g_{KL}'s dynamics confer intensity-invariant spike-time precision only at low stimulus frequencies. *A*: range of vector strengths at different stimulus frequencies. Upper bound is the maximum across all intensities. Lower bound is the minimum across intensities 5 to 50 dB above the intensity yielding maximum vector strength. *B–D*: silicon neuron's membrane responses to a single presentation of a 25-ms, 250-Hz pure tone at 120 dB SPL (*top*). *B*: spike times of all 11 ANF inputs during a single trial (*trial 2* from Fig. 3*B*). *C*: membrane potential with g_{KL} intact (red) or replaced by a static leak (blue). *D*: instantaneous value of g_{KL} conductance.

a static leak the model spiked twice during this same cycle (Fig. 4*C*, blue triangles), because its fixed leak conductance did not increase to reject the second burst of auditory nerve inputs at 15 ms. Thus g_{KL}'s dynamic deactivation and activation conferred the model bushy cell with periodic onset sensitivity. As stimulus frequency increases, the duration of the synaptic silence should decrease proportionally as long as the auditory nerve maintains the same level of spike-time precision. The auditory nerve's vector strength was approximately constant from 250 to 1,000 Hz (Fig. 2*G*), which suggests that the loss of intensity-invariant spike-time precision across this frequency range was strictly due to a reduction in the duration of synaptic silence (and not due to off-phase inputs). Previous studies have indicated that g_{KL} deactivation facilities spikes that follow a brief hyperpolarization of the membrane voltage, whether hyperpolarization is due to a momentary reduction of input current (Day et al. 2008; Gai et al. 2009) or brief inhibition (Dodla et al. 2006), and that spike facilitation is critically dependent on both the timing of such hyperpolarization and g_{KL}'s kinetics. We conclude that the frequency-dependent decline of intensity-invariant spike-time precision (Fig. 4*A*, vertical range of red-shaded region) is due to the kinetics of g_{KL} deactivation: As stimulus frequency increases, the duration of synaptic silence between cycles decreases to the point where g_{KL} cannot fully deactivate before the next cycle.

Amplitude-Modulated High-Frequency Tones

Thus far we have demonstrated the role of g_{KL}'s dynamics in bushy cells most sensitive to low-frequency sounds, but many bushy cells are most sensitive to high frequencies. In this section we identify a role for g_{KL}'s dynamics in these neurons. Bushy cells phase lock less precisely than auditory nerve fibers to pure tones above 1 kHz (see Fig. 2*G*); therefore, g_{KL}'s role is not simply to enhance a neuron's phase locking at its best frequency. A role for g_{KL} in high best-frequency bushy cells may be inferred from various experimental observations. Neurons downstream of bushy cells phase lock to the envelope of amplitude modulation better than auditory nerve fibers, particularly when the stimulus contains periodic silence (Dreyer and Delgutte 2006; Griffin et al. 2005). These studies used half-wave-rectified amplitude modulation of high-frequency tones (half the modulation period is silent) to mimic the waveform-based timing information naturally available to low-frequency channels (van de Par and Kohlrausch 1997). Such stimuli contain onsets, offsets, and periodic silences found in human speech (Rosen 1992); human listeners are better at detecting interaural timing differences between envelopes that contain periodic silence than between classic sine-modulated envelopes (Bernstein and Trahiotis 2002, 2008; van de Par and Kohlrausch 1997). We tested the hypothesis that g_{KL}'s dynamics enables phase locking to half-wave-modulated high-frequency tones across intensities by comparing the simulated responses of an auditory nerve fiber, bushy cell with g_{KL} intact and with a static leak.

g_{KL}'s dynamics conferred the high best-frequency bushy cell with the ability to precisely represent the phase of half-wave modulation across a wide range of intensities. The model bushy cell's spike rate was below 100 spikes/s for all intensity levels, but its vector strength was higher than that of the auditory nerve fiber (Fig. 5*A*). Vector strength remained high as intensity increased only with g_{KL} intact; with a static leak the model's vector strength declined, as did the vector strength of the auditory nerve fiber. This relationship to intensity was similar to the relationship seen with low-frequency pure tones (see Fig. 3*A*), except the vector strengths of all three models were slightly lower with half-wave modulation, especially at the highest intensities. At moderate stimulus intensities, spike rate histograms resulting from half-wave-modulated tones looked nearly identical to those from low-frequency pure tones (compare Fig. 5*B* and Fig. 2, *D–F*). However, at high stimulus intensities, auditory nerve fiber spike rates remained above 0 during a larger fraction of the stimulus period than was observed with low-frequency pure tones (compare Figs. 5*C* and 3*B*), and the bushy cell had some spurious late-phase spikes even with g_{KL} intact. Matched simulations with nonrectified sinusoidal amplitude modulation yielded no differences between bushy cells with g_{KL} intact or replaced by a static leak. Such stimuli drive auditory nerve responses throughout the stimulus cycle (Dreyer and Delgutte 2006), which should eliminate the periodic hyperpolarization of the membrane voltage that triggered periodic g_{KL} deactivation (i.e., Fig. 4, *C* and *D*). We conclude that the periodic silence provided by half-wave rectification was critical for the intensity-invariant spike-time precision imbued by g_{KL}'s dynamics.

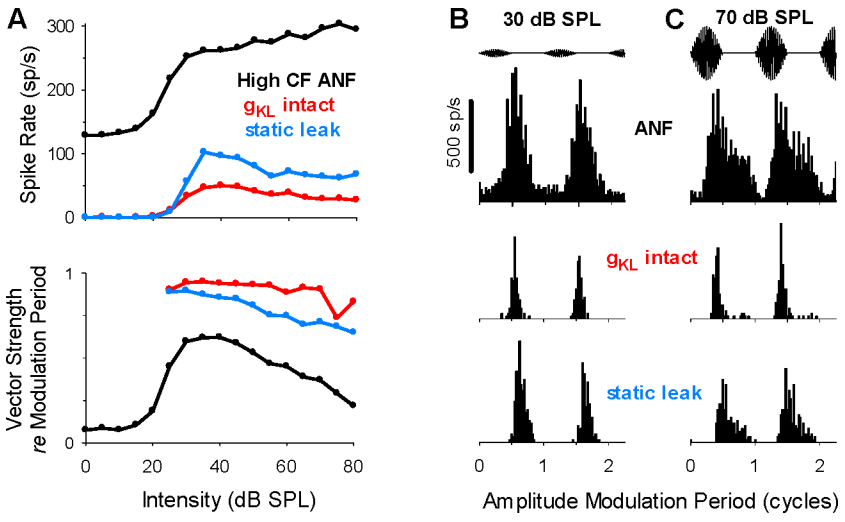

Fig. 5. g_{KL}'s dynamics are necessary for intensity-invariant phase locking to amplitude-modulated high-frequency tones that contain periodic silence. Simulated and in silico responses of high best-frequency auditory neurons to 1,000 repetitions of a 25-ms, 8,000-Hz pure tone, 100% modulated by a 250-Hz half-wave-rectified sinusoid. *A*: driven spike rate and vector strength as in Fig. 3*A*, except spike phases are computed with respect to the envelope rather than the tone. *B* and *C*: stimulus waveforms and spike rate histograms during 2 modulation cycles (12–20 ms after stimulus onset). Vertical scale bar applies to all histograms.

Dynamics of g_{KL} Protect Against Cell-to-Cell Variability

The preceding results demonstrate that g_{KL}'s dynamics are required for intensity-invariant spike-time precision with a particular set of conductance magnitudes and number of auditory nerve inputs. Bushy cells, however, are subject to biophysical variability. They receive different numbers of synaptic inputs with varying strengths and have different maximum values of their voltage-sensitive conductances (Cao et al. 2007). Some heterogeneity can be attributed to differences between bushy cell subtypes (Cao and Oertel 2010). Across all bushy cells, the number of inputs ranges from ~2 to 70 (often between 2 and 24; Ryugo and Sento 1991; Spirou et al. 2005), the strength of individual synapse varies by up to 25-fold (often within 10-fold; cf. Cao and Oertel 2010), and the peak magnitude of g_{KL} varies by up to 4-fold (Cao et al. 2007). Despite significant variability in these biophysical properties, a majority of bushy cells exhibit nearly ideal spike-time precision and spike-count reliability (Joris et al. 1994a). Perhaps consistent responses are achieved through homeostatic mechanisms that enable one biophysical parameter to compensate for another (e.g., g_{KL} and the number of inputs are both high or both low). Alternatively, the responses may be inherently insensitive to biophysical heterogeneity (discussed in Marder 2011).

Cell-to-cell variation does not affect intensity-invariant spike-time precision. We sought to explore the effects of cell-to-cell variability by perturbing model parameters while monitoring spike rate and vector strength across a range of stimulus intensities (Fig. 6*A*). The two parameters we varied were the number of synaptic inputs (from 4 to 32) and the magnitude of g_{KL} (from 0.5- to 2-fold). When varying one parameter, we kept the other at a constant reference level. Compared with the original (average) bushy cell model (see Fig. 3), the reference model's number of inputs was increased to 16 (4 LSR, 4 MSR, and 8 HSR fibers), its synaptic strength was reduced, and its g_{KL} magnitude was the same. These reference settings yielded rate-intensity and vector strength-intensity relationships similar to those that were observed with the original model (compare red points in Figs. 6 and 3*A*). The reference number of inputs was changed to facilitate halving and doubling the number of HSR fibers, and the synaptic strength was set low enough to cause less than ideal spike rates (~235 instead of 250 spikes/s), thereby providing sensitivity to either improvement or degradation of intensity-invariant spike-time precision as each parameter varied.

Cell-to-cell variation did not affect intensity-independent spike-time precision. However, each parameter affected the model bushy cell's spike rate. Rate was higher with more inputs, stronger individual synapses, and less g_{KL}. The biggest changes were in the model's driven rate (>80 dB SPL), although spontaneous rate also varied. In contrast, the model's spike-time precision was nearly ideal as intensity increased in almost all cases. For instance, when driven by 4 nerve fibers instead of 32, the model's driven spike rate dropped from 250 to 50 spikes/s, but its vector strength remained above 0.99 irrespective of intensity in both cases. Variation in the number of inputs and magnitude of g_{KL} did affect the model's ability to fire a single spike each and every stimulus cycle, but the spikes that did occur remained precisely phase locked to the stimulus irrespective of intensity. With g_{KL}, the model bushy cell had consistent spike-time precision despite variation in the number of inputs and magnitude of voltage-sensitive conductances: the response was insensitive to biophysical heterogeneity.

Cell-to-cell variation is detrimental without the dynamics of g_{KL}. Replacing g_{KL} with a static leak increased the model's sensitivity to variation in number of inputs and magnitude of the static leak (Fig. 6*B*). We varied each model parameter over the same range as with g_{KL} intact, but resultant spike rates covered a wider range. For each varied parameter, the lowest driven rates were near 0 and the highest exceeded 275 spikes/s. Similarly, vector strength varied wildly between model permutations. In most conditions spike-time precision declined with stimulus intensity, although three permutations yielded nearly ideal vector strength as stimulus intensity increased (Fig. 6*B*, *left*: ~2 times passive leak; *right*: 8 HSR inputs, 16 HSR

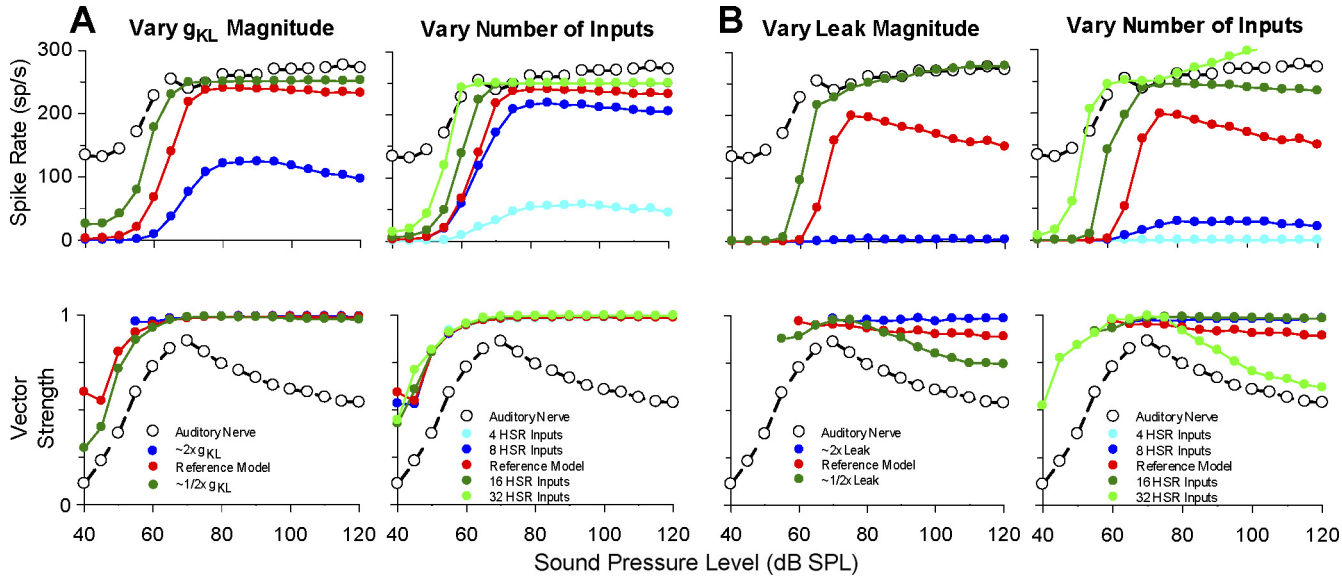

Fig. 6. g_{KL}'s dynamics imbue intensity-invariant spike-time precision despite biophysical heterogeneity. *A* and *B*: parameter dependence (see key) of silicon bushy cell's spike rate and vector strength with g_{KL} intact (*A*) or replaced by a static leak (*B*). Auditory nerve data are provided for comparison (open circles). The reference model is driven by 16 fibers (4 LSR, 4 MSR, and 8 HSR); vector strength is computed only if 10 or more spikes occurred.

inputs), but only one of those had a spike rate sufficiently high for nearly ideal entrainment (16 HSR inputs; entrainment index > 0.95). The static leak was capable of imbuing intensity-invariant spike-time precision only with a few combinations of synaptic input counts and conductance magnitudes. The increased sensitivity to variability with a static leak demonstrates that g_{KL}'s dynamics are essential not only for spike-time precision as stimulus intensity varies but also as specific biophysical attributes are varied in isolation.

Heterogeneity across the silicon microchip is detrimental without the dynamics of g_{KL}. To systematically explore the existence of combinations of synaptic inputs and conductance magnitudes that yield intensity-invariant spike-time precision, we took advantage of the microchip's heterogeneous population of silicon bushy cells. All data reported thus far came from a single silicon bushy cell, but the silicon microchip contains 1,080 bushy cells with nominally identical transistor circuits. When we configured the single silicon bushy cell to have g_{KL} intact or replaced by a static leak, all other silicon bushy cells were similarly configured but with measurable differences in each cell's voltage-dependent conductances due to variation in the conductivity of individual transistors introduced by the fabrication process (de Gyvez and Tuinhout 2004; Pavasović et al. 1994). This transistor-level variability affected each aspect of the cell's conductance equation independently, including conductance magnitudes, kinetics, and voltage dependencies. For instance, the conductance-voltage curve of the silicon bushy cell physically neighboring the one presented earlier has a 15% higher g_{KL} conductance and 20% lower g_{NA} conductance (Fig. 7*A*, compare solid and dotted lines). On average, the conductance-voltage curves of the silicon bushy cell population resembled those of the individual neuron presented in Fig. 2 with a range of approximately ±20% (Fig. 7*A*, shaded region indicates ±2 SD).

g_{KL}'s dynamics protected the population of silicon bushy cells against variability due to transistor mismatch. When driven with a 250-Hz pure tone at 80 dB SPL, the population of 1,080 silicon bushy cells with g_{KL} intact had a narrow range of spike rates centered around 250 spikes/s, the rate required for ideal entrainment (Fig. 7*B*, *inset*: 10th, 50th, and 90th percentiles were 213, 250, and 257 spikes/s, respectively). Vector strengths were narrowly distributed around 0.98 at this stimulus intensity (*top* histogram: 0.97, 0.98, and 0.99). Most neurons maintained a similarly high level of precision at 120 dB SPL (*right* histogram: 0.94, 0.97, and 0.98). Vector strengths at the two intensities were positively correlated; neurons at the lower end of the vector strength distribution at 80 dB were also at the lower end at 120 dB SPL. With g_{KL} intact, biophysical heterogeneity emulated with transistor mismatch causes little variation in driven spike rate, spike count reliability, and intensity-invariant spike-time precision.

The population's response to acoustic stimulation degrades when g_{KL} was replaced by a static leak (Fig. 7*C*). The distribution of driven rates ranged widely, although it also peaked at the rate required for ideal enhancement (*inset*: 10th, 50th, and 90th percentiles were 116, 228, and 314 spikes/s, respectively). Similarly, the distribution of vector strengths at 80 and 120 dB SPL were wider than with g_{KL} intact, with some neurons enhancing spike-time precision at both intensities and others dropping below the vector strength of auditory nerve fibers (0.73, 0.90, 0.96 and 0.51, 0.80, 0.93). The 5% of neurons that maintained near-ideal vector strength at both stimulus intensities had driven rates below 50 spikes/s and therefore did not entrain to the stimulus (light blue points). Neurons with a driven rate appropriate for entrainment exhibited an intensity-dependent decline in vector strength (average drop of 0.1; dark orange points). Neurons with even higher driven rates at 80 dB SPL exhibited a greater decline in vector strength as intensity increased (0.25 for rates >300 spikes/s). With a static leak, biophysical heterogeneity emulated with transistor mismatch led to a wide range of sound-driven responses, but not one of the 1,080 silicon neurons exhibited the combination of intensity-independent spike-time precision and spike-count reliabil-

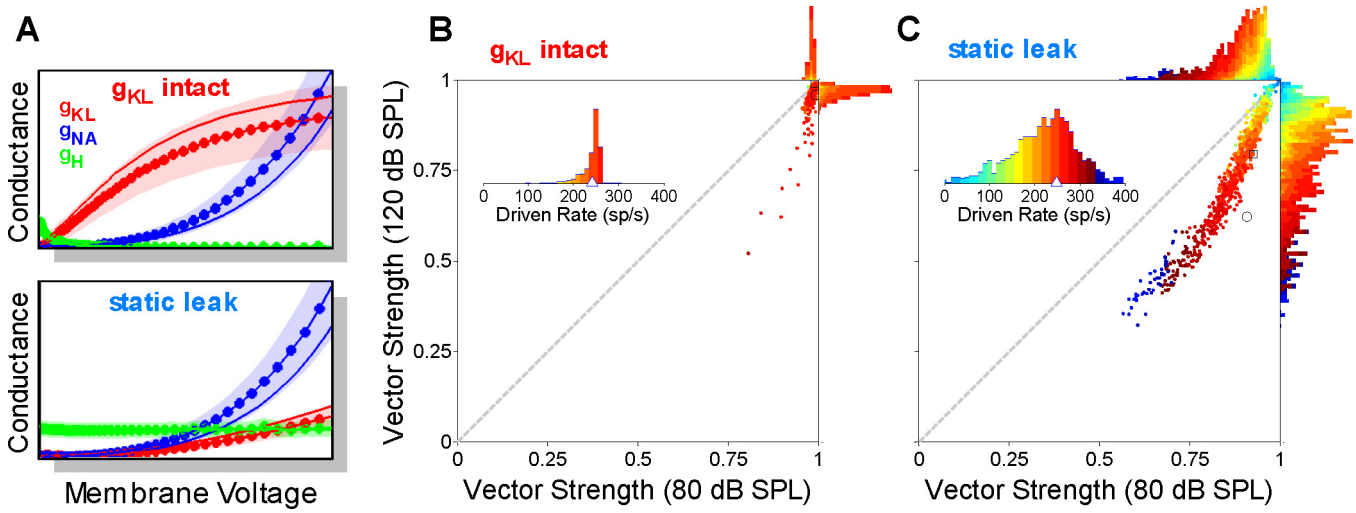

Fig. 7. g_{KL}'s dynamics protect against heterogeneity in a population of 1,080 silicon bushy cells. *A*: conductance-voltage curves' range of variation. Shaded region represents mean ± 2 SD; continuous line is from a silicon bushy cell next to the one shown in Fig. 2, *B* and *C*. *B* and *C*: plot of each cell's vector strength at 80 dB SPL vs. its vector strength at 120 dB SPL, with g_{KL} intact (*B*) or replaced by a static leak (*C*). Respective distributions of vector strengths (*top* and *right* histograms) and driven rates at 80 dB SPL (*insets*) are shown, color-coded on the basis of driven rate. Stimulus and model parameters are identical to those in Fig. 3. Values for the silicon neuron from Figs. 2–6 are indicated with triangles (rate) and squares (vector strength). Vector strengths from the software bushy cell with g_{KL} intact (as in Fig. 2*A*) or fixed at its steady-state level are indicated with circles.

ity that is the signature response of more than 75% of low best-frequency bushy cells in vivo.

DISCUSSION

Summary of Findings

Bushy cells' intensity-invariant spike-time precision and spike-count reliability rely on a key biophysical specialization, the dynamic activation and deactivation of g_{KL} each cycle of an acoustic stimulus. In vitro, g_{KL} conducts even when the neuron is at rest, passing sufficient current to match the depolarizing current passed by the slowly activating conductance g_H. The resting levels of g_{KL} and g_H imbue the bushy cell with a short membrane time constant, which can enable nearly ideal spike-time precision over a narrow range of stimulus intensities, synaptic configurations, and conductance levels (Figs. 6 and 7). However, g_{KL}'s dynamic activation and deactivation, synchronized with sound pressure change (Fig. 4), is required for consistent spike-time precision despite variation in stimulus intensity and biophysical heterogeneity. The role of g_{KL}'s dynamics holds for low-frequency pure tones (Fig. 3) and high-frequency amplitude-modulated tones that include periodic silence to facilitate g_{KL} deactivation (Fig. 5).

Enhancement of Phase Locking

The phenomenal ability of bushy cells to represent the phase of an acoustic stimulus with more precision and better entrainment than their auditory nerve fiber inputs is well documented and has enjoyed substantial theoretical study. Joris et al. (1994a) reported that most low-frequency bushy cells had higher vector strength and entrainment indices than any auditory nerve fiber. An earlier study hinted at this finding with a small set of low-frequency cells (Blackburn and Sachs 1989). Several modeling studies have successfully replicated features of this enhancement phenomenon (reviewed by Joris and Smith 2008). Often they assume the bushy cell takes advantage of its short membrane time constant (Oertel 1983) to detect coincidence of several relatively weak synaptic inputs (Joris et al. 1994a; Rothman and Manis 2003c; Rothman and Young 1996; Xu-Friedman and Regehr 2005a). However, some have assumed an alternative computation of detecting the first of a few strong synaptic inputs, which requires dynamic activation of g_{KL} to limit responses to late inputs (Rothman et al. 1993; Xu-Friedman and Regehr 2005b). These alternates may both come into play across the heterogeneous population of bushy cells, where variation in the number and strength of inputs could bias a cell to one computation or another. The degree of enhancement is therefore argued to depend on a complex interplay of number of synaptic inputs, their amplitudes, and their temporal distribution (Joris and Smith 2008). These models successfully replicate the ability of bushy cells to enhance spike-time precision over some range of model and stimulus parameters. Our bushy cell model successfully enhances spike-time precision with or without g_{KL}'s dynamics over a limited range of stimulus intensities and biophysical parameters.

Intensity Independence of Phase Locking

We are the first to systematically explore the intensity independence of bushy cell spike-time precision and spike-count reliability relative to that of auditory nerve fibers at elevated sound pressure levels, although evidence of this phenomenon is peppered throughout the literature. Often spike-time precision is reported for a single stimulus intensity; thus evidence of intensity-independent spike-time precision comes from the few cells where precision at multiple elevated intensities was reported. Those bushy cells initially increase their spike rate and vector strength at low sound levels and then maintain nearly ideal spike-time precision over a 20- to 30-dB SPL range (Bourk 1976; Joris et al. 1994a; Joris and Smith 2008; Rhode 2008; Smith and Rhode 1987). In contrast, auditory nerve fiber spike-time precision often decreases from its peak value as intensity increases (Palmer and Russell 1986) due to a combination of wider period histograms and intensity-dependent peak splitting that occurs in more than 50% of low-frequency auditory nerve fibers (Cai and Geisler 1996). Often measurements of auditory nerve fiber vector strength miss this because intensity is not increased beyond rate saturation (e.g., Johnson 1980). We drove the silicon bushy cell with an established auditory nerve model (Sumner et al. 2003) that accurately mimicked intensity-dependent decline of phase locking; the model fiber's vector strength declined by 0.23 to 0.32 as intensity increased by 50 dB. Other bushy cell models were driven by idealizations of pure tones using noisy sinusoidal currents (Day et al. 2008; Gai et al. 2009, 2010; Svirskis et al. 2002; Svirskis and Rinzel 2003) or auditory nerve inputs synthesized with a single temporal distribution that did not match any particular sound pressure level (Rothman and Young 1996; Xu-Friedman and Regehr 2005b). These modeling studies have provided rich insight into g_{KL}'s effect on the dynamic properties of bushy cells across a range of stimulus frequencies and noise levels. We uncovered a biophysical mechanism underlying the coding of high-intensity sounds by using auditory nerve inputs that mimicked the response to a range of acoustic stimuli.

Predictions for In Vitro Experiments

The simulation results presented in this article predict that g_{KL}'s dynamics are critical in vivo for the bushy cell's intensity-independent spike-time precision. In theory, this prediction could be confirmed experimentally using in vivo patch clamp during acoustic stimulation, with local application of dendrotoxin to block g_{KL} and dynamic clamp to introduce a static leak (e.g., Nagtegaal and Borst 2010). A slightly less challenging experimental confirmation would use in vitro patch clamp, again with dendrotoxin and dynamic clamp; however, in this case the dynamic clamp would additionally be used to introduce synthetic synaptic conductances generated from an established auditory nerve model (e.g., Prinz et al. 2003b). Both of these proposed experimental confirmations rely on synaptic inputs from the auditory nerve, whether real or synthetic, to study the effects of sound intensity on spike-time precision. A more rarified in vitro experiment might instead use noisy sinusoidal currents to represent an idealization of the synaptic input during acoustic stimulation. This approach would not accurately reflect the decrease in auditory nerve spike-time precision as intensity increases (e.g., bimodal period histograms due to peak splitting), and therefore it would not be appropriate for confirming that g_{KL}'s dynamics are critical for intensity-independent spike-time precision. How-

ever, the sinusoidal idealization could be used to test the hypothesis that a gap of silence is important for encoding amplitude-modulated sounds and, moreover, that the duration of that gap is critically dependent on the time course of g_{KL} deactivation. On the basis of the findings reported presently, we predict that a bushy cell in vitro would phase lock more precisely with g_{KL}'s dynamics intact only if the stimulus includes a gap of silence sufficiently long to allow for g_{KL}'s deactivation between cycles.

Neuromorphic vs. Software Modeling

A key feature of neuromorphic modeling, real-time simulation, facilitated our exploration of a wide range of different stimulus and model parameters that eventually led to the findings reported here. We initially observed the effects of g_{KL}'s dynamics on spike-time precision by concurrently monitoring spike-rasters and phase-histograms of three silicon bushy cells while adjusting input and model parameters on the fly (see Fig. 1*B*). Modeling in silicon offers several benefits over software, such as low power consumption, a small physical footprint, and parallel computation of each neuron's circuit equation so that large populations of neurons can be modeled without increasing simulation time. Modeling in silicon also has drawbacks compared with software, such as a slow development period (chip design and fabrication takes several months), the need to simplify model equations so they can be approximated with transistor circuits, and intrinsic variation between silicon neurons due to transistor-transistor mismatch. These last two points make it difficult to reproduce the response properties of any particular silicon neuron and therefore made us concerned that the intensity-independent spike-time precision we observed with the silicon bushy cell was simply an unintended consequence of the modeling technique. To allay this concern, we repeated the simulations using an established software model of the bushy cell (Rothman and Manis 2003c). The software bushy cell model replicated our findings in silicon, displaying intensity-invariant spike-time precision with g_{KL} intact (Fig. 7, compare circles in *B* and *C*) and susceptibility to changes in the number or strength of synaptic inputs when g_{KL} was replaced with a static leak. Therefore, in principle, the present results could have been uncovered and reported exclusively using a software model.

Subtypes of Bushy Cells and Cell-to-Cell Variation

Throughout the RESULTS section we referred to the model generically as a bushy cell, but in fact there are two distinct subtypes of bushy cells, globular and spherical, that have different distributions of synaptic convergence and conductance magnitudes as well as distinct axonal targets (Smith et al. 1991, 1993). On average, globular bushy cells are innervated by more auditory nerve fibers than spherical cells. Anatomic measurements from cats indicate that globular bushy cells are innervated by between 9 and 69 somatic inputs, with a median of about 19 (Spirou et al. 2005), whereas spherical bushy cells are innervated by between 1 and 3 (Brawer and Morest 1975; Ryugo and Sento 1991). Physiological estimates from the mouse indicate that globular bushy cells receive four or more inputs, whereas spherical bushy cells receive three or fewer (Cao and Oertel 2010). The average size of auditory nerve boutons is smaller on globular bushy cell somas compared with spherical, suggesting different effective strengths of each synapse. Globular bushy cells often have twofold greater g_{KL} magnitude (Cao et al. 2007). Although there is significant variation in these parameters between cell types, there is also substantial variation of these (and other) parameters within cell types (Cao and Oertel 2010; Rothman and Manis 2003a).

To test the effect of these differences on our model, we systematically varied the number of synaptic inputs and leak conductance magnitudes to encompass the variation observed within and between globular and spherical bushy cells (Fig. 6). In almost all conditions the model with g_{KL} intact retained its intensity-invariant spike-time precision, which is consistent with the observation that a majority of both globular and spherical bushy cells exhibit this unique phenomenon. With g_{KL} intact, the bushy cell's response was insensitive to biophysical variation, as is sometimes seen in other neural circuits subject to variability (Prinz et al. 2003a). In contrast, with g_{KL} replaced by a static leak, the bushy cell achieved intensity-invariant spike-time precision with only a few combinations of synaptic inputs and conductances. Such combinations are also observed in other neural circuits (Taylor et al. 2009), where desired neural responses are achieved with disparate mixtures of biophysical parameters. Some neural circuits maintain consistent functionality despite variability in a conductance's magnitude by compensatory changes within a cell (Goaillard et al. 2009; MacLean et al. 2003) or across synapses within a local network (Grashow et al. 2010). We demonstrated that g_{KL}'s dynamics protect the bushy cell from heterogeneity without requiring homeostatic compensation of other conductances within the cell or synaptic changes within the local network. The protection extended to a large population of silicon neurons whose biophysical heterogeneity was emulated with transistor mismatch, therefore addressing a fundamental design constraint in neuromorphic engineering.

Other g_{KL}-Expressing Neurons

The stability of the model's response over such a wide range of acoustic and biophysical parameters suggests that other auditory neurons with g_{KL} have the capacity for robust spike-time precision. Several cell types besides bushy cells possess g_{KL} and have precisely timed spikes, including spiral ganglion cells of the auditory nerve (Adamson et al. 2002; Santos-Sacchi 1993), octopus cells of the cochlear nucleus (Bal and Oertel 2001), and principal neurons of the medial nucleus of the trapezoid body (Klug and Trussell 2006) and the medial superior olive (Grothe and Sanes 1994; Svirskis et al. 2002). Most of these cell types have g_{KL} magnitudes and synapse counts within the ranges observed for bushy cells; therefore, we predict their spike-time precision is insensitive to acoustic and biophysical variability. However, two of these cell types (spiral ganglion and principal neurons of the medial nucleus of the trapezoid body) are innervated by a single input, which raises the question of whether spike-time precision can be enhanced without the convergence multiple inputs. Our results indicate that if the single input spikes more than once per stimulus cycle, g_{KL} could suppress a response to the subsequent, off-phase spikes. Furthermore, these single synaptic inputs are composed of multiple coordinated but independent readily releasable vesicles (Borst and Sakmann 1996; Neef et al. 2007) with a heterogeneous distribution of release times

(Meinrenken et al. 2002; Wittig and Parsons 2008), which essentially increases the number of functional inputs to within the range observed for bushy cells.

ACKNOWLEDGMENTS

We thank Donata Oertel for many thoughtful discussions about bushy cells and a critical reading of an early version of the manuscript.

GRANTS

This work was supported by National Institute on Deafness and Other Communication Disorders Grant T32 DC 005363 (fellowship to J. H. Wittig, Jr.), the MOSIS Educational Program (chip fabrication), and Packard Foundation Grant 99-1454.

DISCLOSURES

No conflicts of interest, financial or otherwise, are declared by the authors.

AUTHOR CONTRIBUTIONS

J.H.W. and K.B. conception and design of research; J.H.W. performed experiments; J.H.W. analyzed data; J.H.W. and K.B. interpreted results of experiments; J.H.W. prepared figures; J.H.W. drafted manuscript; J.H.W. and K.B. edited and revised manuscript; J.H.W. and K.B. approved final version of manuscript.

REFERENCES

Adamson CL, Reid MA, Mo ZL, Bowne-English J, Davis RL. Firing features and potassium channel content of murine spiral ganglion neurons vary with cochlear location. *J Comp Neurol* 447: 331–350, 2002.

Bal R, Oertel D. Potassium currents in octopus cells of the mammalian cochlear nucleus. *J Neurophysiol* 86: 2299–2311, 2001.

Bernstein LR, Trahiotis C. Discrimination of interaural temporal disparities conveyed by high-frequency sinusoidally amplitude-modulated tones and high-frequency transposed tones: effects of spectrally flanking noises. *J Acoust Soc Am* 124: 3088–3094, 2008.

Bernstein LR, Trahiotis C. Enhancing sensitivity to interaural delays at high frequencies by using "transposed stimuli". *J Acoust Soc Am* 112: 1026–1036, 2002.

Blackburn CC, Sachs MB. Classification of unit types in the anteroventral cochlear nucleus: PST histograms and regularity analysis. *J Neurophysiol* 62: 1303–1329, 1989.

Boahen KA. A burst-mode word-serial address-event channel. *IEEE Trans Circuits Syst I Regul Pap* 51: 1269–1300, 2004.

Borst JG, Sakmann B. Calcium influx and transmitter release in a fast CNS synapse. *Nature* 383: 431–434, 1996.

Bourk TR. *Electrical Response of Neural Units in the Anteroventral Cochlear Nucleus of the Cat* **(PhD thesis).** Cambridge, MA: Massachusetts Institute of Technology, 1976.

Brawer JR, Morest DK. Relations between auditory nerve endings and cell types in the cat's anteroventral cochlear nucleus seen with the Golgi method and Nomarski optics. *J Comp Neurol* 160: 491–506, 1975.

Burkitt AN, Clark GM. Synchronization of the neural response to noisy periodic synaptic input. *Neural Comput* 13: 2639–2672, 2001.

Cai Y, Geisler CD. Temporal patterns of the responses of auditory-nerve fibers to low-frequency tones. *Hear Res* 96: 83–93, 1996.

Cao XJ, Oertel D. Auditory nerve fibers excite targets through synapses that vary in convergence, strength, and short-term plasticity. *J Neurophysiol* 104: 2308–2320, 2010.

Cao XJ, Oertel D. The magnitudes of hyperpolarization-activated and low-voltage-activated potassium currents co-vary in neurons of the ventral cochlear nucleus. *J Neurophysiol* 106: 630–640, 2011.

Cao XJ, Shatadal S, Oertel D. Voltage-sensitive conductances of bushy cells of the mammalian ventral cochlear nucleus. *J Neurophysiol* 97: 3961–3975, 2007.

Day ML, Doiron B, Rinzel J. Subthreshold K^+ channel dynamics interact with stimulus spectrum to influence temporal coding in an auditory brain stem model. *J Neurophysiol* 99: 534–544, 2008.

de Gyvez JP, Tuinhout HP. Threshold voltage mismatch and intra-die leakage current in digital CMOS circuits. *IEEE J Solid-State Circuits* 39: 157–168, 2004.

Dodla R, Svirskis G, Rinzel J. Well-timed, brief inhibition can promote spiking: postinhibitory facilitation. *J Neurophysiol* 95: 2664–2677, 2006.

Dreyer A, Delgutte B. Phase locking of auditory-nerve fibers to the envelopes of high-frequency sounds: implications for sound localization. *J Neurophysiol* 96: 2327–2341, 2006.

Fisher NI. *Statistical Analysis of Circular Data*. Cambridge, UK: Cambridge University Press, 1995, p. 277.

Gai Y, Doiron B, Kotak V, Rinzel J. Noise-gated encoding of slow inputs by auditory brain stem neurons with a low-threshold K^+ current. *J Neurophysiol* 102: 3447–3460, 2009.

Gai Y, Doiron B, Rinzel J. Slope-based stochastic resonance: how noise enables phasic neurons to encode slow signals. *PLoS Comput Biol* 6: e1000825, 2010.

Gittelman JX, Tempel BL. Kv1.1-containing channels are critical for temporal precision during spike initiation. *J Neurophysiol* 96: 1203–1214, 2006.

Goaillard JM, Taylor AL, Schulz DJ, Marder E. Functional consequences of animal-to-animal variation in circuit parameters. *Nat Neurosci* 12: 1424–1430, 2009.

Golding NL, Ferragamo MJ, Oertel D. Role of intrinsic conductances underlying responses to transients in octopus cells of the cochlear nucleus. *J Neurosci* 19: 2897–2905, 1999.

Grashow R, Brookings T, Marder E. Compensation for variable intrinsic neuronal excitability by circuit-synaptic interactions. *J Neurosci* 30: 9145–9156, 2010.

Griffin SJ, Bernstein LR, Ingham NJ, McAlpine D. Neural sensitivity to interaural envelope delays in the inferior colliculus of the guinea pig. *J Neurophysiol* 93: 3463–3478, 2005.

Grothe B, Sanes DH. Synaptic inhibition influences the temporal coding properties of medial superior olivary neurons: an in vitro study. *J Neurosci* 14: 1701–1709, 1994.

Johnson DH. The relationship between spike rate and synchrony in responses of auditory-nerve fibers to single tones. *J Acoust Soc Am* 68: 1115–1122, 1980.

Joris PX, Carney LH, Smith PH, Yin TC. Enhancement of neural synchronization in the anteroventral cochlear nucleus. I Responses to tones at the characteristic frequency. *J Neurophysiol* 71: 1022–1036, 1994a.

Joris PX, Smith PH. The volley theory and the spherical cell puzzle. *Neuroscience* 154: 65–76, 2008.

Joris PX, Smith PH, Yin TC. Enhancement of neural synchronization in the anteroventral cochlear nucleus. II Responses in the tuning curve tail. *J Neurophysiol* 71: 1037–1051, 1994b.

Kalluri S, Delgutte B. Mathematical models of cochlear nucleus onset neurons. II. Model with dynamic spike-blocking state. *J Comput Neurosci* 14: 91–110, 2003.

Klug A, Trussell LO. Activation and deactivation of voltage-dependent K^+ channels during synaptically driven action potentials in the MNTB. *J Neurophysiol* 96: 1547–1555, 2006.

Liberman MC. Central projections of auditory-nerve fibers of differing spontaneous rate. I. Anteroventral cochlear nucleus. *J Comp Neurol* 313: 240–258, 1991.

MacLean JN, Zhang Y, Johnson BR, Harris-Warrick RM. Activity-independent homeostasis in rhythmically active neurons. *Neuron* 37: 109–120, 2003.

Manis PB, Marx SO. Outward currents in isolated ventral cochlear nucleus neurons. *J Neurosci* 11: 2865–2880, 1991.

Marder E. Variability, compensation, and modulation in neurons and circuits. *Proc Natl Acad Sci USA* 108, *Suppl* 3: 15542–15548, 2011.

Mead C. *Analog VLSI and Neural Systems*. Reading, MA: Addison-Wesley, 1989, p. xxii, 371, [378] of plates.

Meinrenken CJ, Borst JG, Sakmann B. Calcium secretion coupling at calyx of Held governed by nonuniform channel-vesicle topography. *J Neurosci* 22: 1648–1667, 2002.

Nagtegaal AP, Borst JG. In vivo dynamic clamp study of I_h in the mouse inferior colliculus. *J Neurophysiol* 104: 940–948, 2010.

Neef A, Khimich D, Pirih P, Riedel D, Wolf F, Moser T. Probing the mechanism of exocytosis at the hair cell ribbon synapse. *J Neurosci* 27: 12933–12944, 2007.

Oertel D. Synaptic responses and electrical properties of cells in brain slices of the mouse anteroventral cochlear nucleus. *J Neurosci* 3: 2043–2053, 1983.

Oertel D, Wright S, Cao XJ, Ferragamo M, Bal R. The multiple functions of T stellate/multipolar/chopper cells in the ventral cochlear nucleus. *Hear Res* 276: 61–69, 2011.

Palmer AR, Russell IJ. Phase-locking in the cochlear nerve of the guinea-pig and its relation to the receptor potential of inner hair-cells. *Hear Res* 24: 1–15, 1986.

Pavasović A, Andreou A, Westgate C. Characterization of subthreshold MOS mismatch in transistors for VLSI systems. *J Signal Process Syst* 8: 75–85, 1994.

Prinz AA, Thirumalai V, Marder E. The functional consequences of changes in the strength and duration of synaptic inputs to oscillatory neurons. *J Neurosci* 23: 943–954, 2003a.

Prinz AA, Thirumalai V, Marder E. The functional consequences of changes in the strength and duration of synaptic inputs to oscillatory neurons. *J Neurosci* 23: 943–954, 2003b.

Rhode WS. Response patterns to sound associated with labeled globular/bushy cells in cat. *Neuroscience* 154: 87–98, 2008.

Rhode WS, Smith PH. Characteristics of tone-pip response patterns in relationship to spontaneous rate in cat auditory nerve fibers. *Hear Res* 18: 159–168, 1985.

Rhode WS, Smith PH. Encoding timing and intensity in the ventral cochlear nucleus of the cat. *J Neurophysiol* 56: 261–286, 1986.

Rosen S. Temporal information in speech: acoustic, auditory and linguistic aspects. *Philos Trans R Soc Lond B Biol Sci* 336: 367–373, 1992.

Rothman JS, Manis PB. Differential expression of three distinct potassium currents in the ventral cochlear nucleus. *J Neurophysiol* 89: 3070–3082, 2003a.

Rothman JS, Manis PB. Kinetic analyses of three distinct potassium conductances in ventral cochlear nucleus neurons. *J Neurophysiol* 89: 3083–3096, 2003b.

Rothman JS, Manis PB. The roles potassium currents play in regulating the electrical activity of ventral cochlear nucleus neurons. *J Neurophysiol* 89: 3097–3113, 2003c.

Rothman JS, Young ED. Enhancement of neural synchronization in computational models of ventral cochlear nucleus bushy cells. *Aud Neurosci* 2: 47–62, 1996.

Rothman JS, Young ED, Manis PB. Convergence of auditory nerve fibers onto bushy cells in the ventral cochlear nucleus: implications of a computational model. *J Neurophysiol* 70: 2562–2583, 1993.

Ryugo DK, Sento S. Synaptic connections of the auditory nerve in cats: relationship between endbulbs of held and spherical bushy cells. *J Comp Neurol* 305: 35–48, 1991.

Santos-Sacchi J. Voltage-dependent ionic conductances of type I spiral ganglion cells from the guinea pig inner ear. *J Neurosci* 13: 3599–3611, 1993.

Smith PH, Joris PX, Carney LH, Yin TC. Projections of physiologically characterized globular bushy cell axons from the cochlear nucleus of the cat. *J Comp Neurol* 304: 387–407, 1991.

Smith PH, Joris PX, Yin TC. Projections of physiologically characterized spherical bushy cell axons from the cochlear nucleus of the cat: evidence for delay lines to the medial superior olive. *J Comp Neurol* 331: 245–260, 1993.

Smith PH, Rhode WS. Characterization of HRP-labeled globular bushy cells in the cat anteroventral cochlear nucleus. *J Comp Neurol* 266: 360–375, 1987.

Spirou GA, Rager J, Manis PB. Convergence of auditory-nerve fiber projections onto globular bushy cells. *Neuroscience* 136: 843–863, 2005.

Sumner CJ, O'Mard LP, Lopez-Poveda EA, Meddis R. A nonlinear filter-bank model of the guinea-pig cochlear nerve: rate responses. *J Acoust Soc Am* 113: 3264–3274, 2003.

Svirskis G, Kotak V, Sanes DH, Rinzel J. Enhancement of signal-to-noise ratio and phase locking for small inputs by a low-threshold outward current in auditory neurons. *J Neurosci* 22: 11019–11025, 2002.

Svirskis G, Rinzel J. Influence of subthreshold nonlinearities on signal-to-noise ratio and timing precision for small signals in neurons: minimal model analysis. *Network* 14: 137–150, 2003.

Taylor AL, Goaillard JM, Marder E. How multiple conductances determine electrophysiological properties in a multicompartment model. *J Neurosci* 29: 5573–5586, 2009.

van de Par S, Kohlrausch A. A new approach to comparing binaural masking level differences at low and high frequencies. *J Acoust Soc Am* 101: 1671–1680, 1997.

Wittig JH Jr. *Sound Processing in the Brain: Biophysical Mechanisms for Precise Temporal Signaling in the Auditory System*. Saarbrücken, Germany: Lambert Academic, 2010.

Wittig JH Jr, Boahen KA. Silicon neurons that phase-lock. In: *IEEE International Symposium on Circuits and Systems*. Kos, Greece: 2006, p. 4535–4538.

Wittig JH Jr, Parsons TD. Synaptic ribbon enables temporal precision of hair cell afferent synapse by increasing the number of readily releasable vesicles: a modeling study. *J Neurophysiol* 100: 1724–1739, 2008.

Xu-Friedman MA, Regehr WG. Dynamic-clamp analysis of the effects of convergence on spike timing. I. Many synaptic inputs. *J Neurophysiol* 94: 2512–2525, 2005a.

Xu-Friedman MA, Regehr WG. Dynamic-clamp analysis of the effects of convergence on spike timing. II. Few synaptic inputs. *J Neurophysiol* 94: 2526–2534, 2005b.

Yin TC. Neural mechanisms of encoding binaural localization cues in the auditory brainstem. In: *Integrative Functions in the Mammalian Auditory Pathway*, edited by Oertel D, Popper AN, and Ray RR. New York: Springer, 2002, p. 99–159.

Young ED, Oertel D. Cochlear nucleus. In: *The Synaptic Organization of the Brain*, edited by Sheperd GM. Oxford: Oxford University Press, 2004, p. 125–164.

Zahar Y, Reches A, Gutfreund Y. Multisensory enhancement in the optic tectum of the barn owl: spike count and spike timing. *J Neurophysiol* 101: 2380–2394, 2009.